Optics Letters

Talbot effect of azimuthally periodic Bessel-based structures

Davud Hebri,[1] **Mohammad Bagheri,**[1] **and Saifollah Rasouli**[1,2,*] (iD)

[1]*Department of Physics, Institute for Advanced Studies in Basic Sciences (IASBS), Zanjan 45137-66731, Iran*
[2]*Optics Research Center, Institute for Advanced Studies in Basic Sciences (IASBS), Zanjan 45137-66731, Iran*
Corresponding author: rasouli@iasbs.ac.ir

In this work, the theory of self-imaging in the polar coordinates for azimuthally periodic Bessel-based structures (APBBSs) is presented. For the first time, to the best of our knowledge, we define single- and multi-frequency APBBSs and show that these structures have self-images under plane-wave illumination. We also define sinusoidal and binary-like single-frequency APBBSs and theoretically and experimentally investigate the near-field diffraction of these structures. The diffraction from these structures provides 2D arrays of optical traps that can be used in multi-trapping. © 2019 Optical Society of America

https://doi.org/10.1364/OL.44.004355

One of the well-known phenomena observed in the near-field diffraction is the self-imaging phenomenon or so-called Talbot effect [1–6]. In the diffraction of a plane wave from a periodic structure, the light beam distribution immediately after the structure regenerates itself at certain propagation distances. Since in this image formation there is no imaging system, the effect is known as the self-imaging phenomenon. It is worth noting that for pure phase periodic structures, again the Talbot effect occurs, but such definition of the self-imaging is violated. For instance, in the illumination of a phase grating with a plane wave, fractional Talbot images indirectly resemble the input pattern, in which when the input pattern consists of a binary phase grating, the output Fresnel self-image is a binary amplitude version of the same pattern [7]. In general, self-imaging is a result of discrete superposition of nondiffracting beams [8]. The Talbot effect is conventionally known for the periodic structures in Cartesian coordinates. In the polar coordinates, such an effect can be observed by specific designing of the structures. In a number of studies, the self-imaging effect in the polar coordinates was investigated, namely, self-imaging of the evolute circular gratings [9], almost 2D periodic structures [10], and J_0 amplitude transmittance objects [8,11]. In the diffraction from structures having transmittances with no radial dependence, say radial structures [12], the conventional Talbot effect is not observed. However, some interesting phenomena occur in the diffraction from radial structures, including formation of monochromatic and colorful Talbot carpet at

the transverse plane [12,13], possessing Gaussian curvature between the plane boundaries of the optical regimes [12], flow of the light energy toward the optical axis, and formation of an Arago–Poisson spot-like light-bar on the optical axis in the vortex beam illumination [14], and generating spatially asymmetric, nondiffracting, and self-healing radial carpet, petal-like, and twisted-intensity ring-like vortex beams, and 2D optical lattices [15,16].

In this Letter, we show that by adding Bessel functionality to radially periodic structures, they attain a self-imaging property. As these structures are periodic in the azimuthal direction, we call them azimuthally periodic Bessel-based structures (APBBSs). The azimuthal periodicity of these structures characterizes them as simple diffracting elements to produce 2D arrays of optical traps that can be used in multi-trapping. In a similar scheme in the Cartesian system, simultaneous optical trapping of microparticles in multiple planes was previously presented [17].

First we briefly present the mathematical foundation of the work by considering the Fourier transform in the polar coordinate. Considering (r, θ) as the polar coordinates in the spatial domain and (ρ, ϕ) as the corresponding coordinates in the spectral domain, the following properties for the 2D Fourier transform can be verified [18]:

$$\mathcal{F}\{g(r)e^{in\theta}\} = (-i)^n e^{in\phi}\mathcal{H}_n\{g(r)\}, \tag{1a}$$

$$\mathcal{F}^{-1}\{G(\rho)e^{in\phi}\} = (i)^n e^{in\theta}\mathcal{H}_n\{G(\rho)\}, \tag{1b}$$

where $\mathcal{F}$ and $\mathcal{F}^{-1}$, respectively, represent the 2D Fourier transform and its inverse, and $G(\rho)$ and $g(r)$ are related to each other by the Hankel transform of order n, which is defined as follows:

$$\mathcal{H}_n\{g(r)\} = G(\rho) = 2\pi \int_0^\infty rg(r)J_n(2\pi\rho r)\mathrm{d}r, \tag{2a}$$

$$\mathcal{H}_n\{G(\rho)\} = g(r) = 2\pi \int_0^\infty \rho G(\rho)J_n(2\pi\rho r)\mathrm{d}\rho. \tag{2b}$$

It should be noted that, as the Hankel transform and its inverse have the same forms, both of them can be represented by a unique symbol of $\mathcal{H}_n$. Therefore, $g(r)$ and $G(\rho)$ are called a

Hankel transform pair. Using $\mathcal{H}_{-n}\{g(r)\} = (-1)^n \mathcal{H}_n\{g(r)\}$ in Eq. (1), it is easy to show that

$$\mathcal{F}\{g(r)\cos(n\theta)\} = (-i)^n \cos(n\phi)\mathcal{H}_n\{g(r)\}, \qquad \text{(3a)}$$

$$\mathcal{F}^{-1}\{G(\rho)\cos(n\phi)\} = (i)^n \cos(m\theta)\mathcal{H}_n\{G(\rho)\}. \qquad \text{(3b)}$$

Let us now recall the flowing reference identities [19]:

$$\mathcal{H}_n\{J_n(2\pi\rho_0 r)\} = \frac{\delta(\rho - \rho_0)}{2\pi\rho_0}, \qquad \text{(4a)}$$

$$\mathcal{H}_n\left\{\frac{\delta(\rho - \rho_0)}{2\pi\rho_0}\right\} = J_n(2\pi\rho_0 r), \qquad \text{(4b)}$$

where δ indicates the Dirac delta function. Looking at Eq. (4), we see that $g(r) = J_n(2\pi\rho_0 r)$ and $G(\rho) = \frac{\delta(\rho-\rho_0)}{2\pi\rho_0}$ are the Hankel transforms of each other, and they construct a Hankel transform pair. Substituting this Hankel transform pair in Eq. (3), we obtain the following key results:

$$\mathcal{F}\{\cos(n\theta)J_n(2\pi\rho_0 r)\} = (-i)^n \cos(n\varphi)\frac{\delta(\rho - \rho_0)}{2\pi\rho_0}, \qquad \text{(5a)}$$

$$\mathcal{F}^{-1}\left\{\cos(n\varphi)\frac{\delta(\rho - \rho_0)}{2\pi\rho_0}\right\} = (i)^n \cos(n\theta)J_n(2\pi\rho_0 r). \qquad \text{(5b)}$$

Now we utilize this result to investigate near-field diffraction from a single-frequency APBBS. We define a single-frequency APBBS with the following transmission function:

$$t(r,\theta) = c + \sum_{n=0}^{\infty} t_n J_n\left(\frac{2\pi r}{r_0}\right)\cos(n\theta), \qquad \text{(6)}$$

where c and t_n are arbitrary coefficients, and r_0 is a characteristic length. In the passing of a coherent plane wave through this structure, the complex amplitude immediately after the structure is

$$\psi_0(r,\theta) = c + \sum_{n=0}^{\infty} t_n J_n(2\pi\rho_0 r)\cos(n\theta), \qquad \text{(7)}$$

where ρ_0 is the radial spatial frequency of the structure, and its value determines the characteristic length as $r_0 = \frac{1}{\rho_0}$. We used the term "single-frequency" because the defined structure has a unique radial spatial frequency. We use spatial spectrum analysis to predict the diffracted light beam distribution. By taking a 2D Fourier transform of $\psi_0(r,\theta)$, the spatial spectrum of the light beam amplitude at $z = 0$ can be obtained as follows:

$$\tilde{\psi}_0(\rho,\varphi) = c\delta(\xi,\eta) + \sum_{n=0}^{\infty} t_n(-i)^n \cos(n\varphi)\frac{\delta(\rho - \rho_0)}{2\pi\rho_0}, \qquad \text{(8)}$$

where Eq. (5a) is used. This result shows that the spatial spectrum of the structure includes a point impulse on the origin of the spectrum domain and a circular line impulse with a radius of $\rho_0 = \frac{1}{r_0}$ around the spectrum origin.

The free-space transfer function is given by [18]

$$H = H_0 \exp[-i\pi\lambda z(\xi^2 + \eta^2)] = H_0 \exp(-i\pi\lambda z\rho^2), \qquad \text{(9)}$$

where $H_0 = \exp(ikz)$. In the rest of the paper, H_0 is ignored for convenience. Multiplying H to $\tilde{\psi}_0(\rho,\varphi)$, the spatial spectrum of the light beam after a propagation distance z from the structure is obtained by

$$\tilde{\psi}_z(\rho,\varphi) = c\delta(\xi,\eta) + e^{-i\pi\lambda z\rho_0^2}\sum_{n=0}^{\infty} t_n(-i)^n \cos(n\varphi)\frac{\delta(\rho - \rho_0)}{2\pi\rho_0}, \qquad \text{(10)}$$

where we used the Dirac delta function's properties. By taking an inverse Fourier transform from $\tilde{\psi}_z(\rho,\varphi)$, the near-field diffraction amplitude is calculated as

$$\psi_z(r,\theta) = c + e^{-2i\pi\left(\frac{z}{z_t}\right)}\sum_{n=0}^{\infty} t_n J_n(2\pi\rho_0 r)\cos(n\theta), \qquad \text{(11)}$$

where $z_t = \frac{2}{\lambda\rho_0^2} = \frac{2r_0^2}{\lambda}$ can be considered as the structure's Talbot distance. Comparing Eqs. (7) and (11) we see that at distances equal to the integer multiples of z_t, the diffracted amplitude fully recovers its initial shape.

As a simple case of single-frequency APBBSs, here a sinusoidal single-frequency APBBS is introduced by the following transmission function:

$$t(r,\theta) = \frac{1}{2}\left[1 + a_m J_m\left(\frac{2\pi r}{r_0}\right)\cos(m\theta)\right], \qquad \text{(12)}$$

where $a_m = 1/\max\{J_m(x)\}$ is the inverse of the absolute maximum value of mth order Bessel function. Choosing this value for a_m maximizes the contrast of the transmittance. In Fig. 1(a), the transmittance of a sinusoidal single-frequency APBBS is illustrated. Comparing Eqs. (12) and (7), we see that $c = \frac{1}{2}$ and $t_{n=m} = \frac{a_m}{2}$ and other coefficients vanish, say $t_{n\neq m} = 0$. Using these coefficients in Eq. (11), the near-field diffraction pattern of a sinusoidal single-frequency APBBS can be obtained.

In Fig. 2, theoretically predicted and experimentally recorded diffraction patterns from two sinusoidal single-frequency APBBSs with $m = 15$ and having two different values of $r_0 = 0.5$ mm and $r_0 = 1$ mm are illustrated. Patterns of the first and third rows are produced theoretically, and patterns of the second and forth rows are recorded experimentally. To record the experimental patterns, a collimated wavefront of the second harmonic of an Nd:YAG diode-pumped laser beam with a wavelength of $\lambda = 532$ nm is propagated through the structure. The diffracted patterns at different propagation distances from the structure are recorded by a camera (NIKON D7200). In order to have high-resolution diffraction patterns, we remove the imaging lens of the camera, then we record the diffraction patterns directly over the active area of the camera without any magnification in size. The active image area of the camera is 23.5 mm × 15.6 mm. The structure and camera are
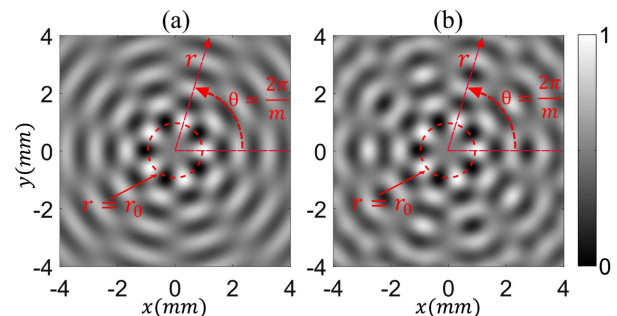

Fig. 1. Transmittance of (a) a sinusoidal and (b) a binary-like single-frequency APBBS with $m = 5$ and $r_0 = 1$ mm.
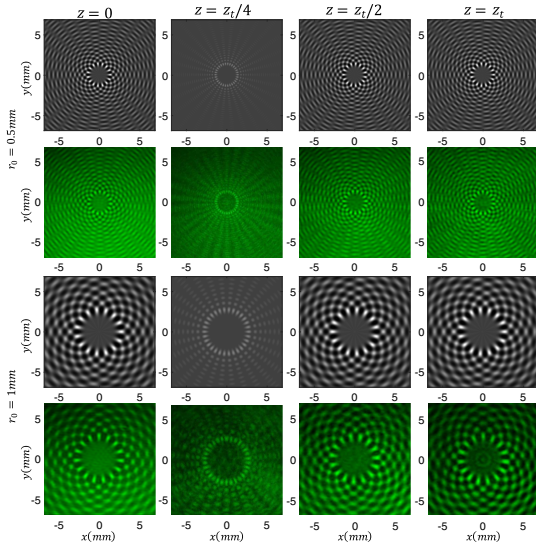
Fig. 2. Calculated (first and third rows) and experimentally recorded (second and fourth rows) intensity diffraction patterns at different propagation distances from sinusoidal single-frequency APBBSs with $m = 15$ and having different values of $r_0 = 0.5$ mm and $r_0 = 1$ mm (see Visualization 1).

installed in the setup in which their planes are perpendicular to the propagation direction. The structures are constructed by a lithography method on transparent plates with a spatial resolution of 300 dpi. The diameter of the constructed structures is 40 mm. In the experiments, they are fully illuminated by a uniform laser beam. A square area of the recorded patterns are grabbed and illustrated in the figures.

As is apparent in Fig. 2, at $z = z_t$, the resulting patterns are self-images, and at $z = \frac{z_t}{2}$, we have self-images with a π phase shift with respect to the corresponding patterns at $z = 0$. The central bright spots form a petal-like pattern over the self-imaging planes. At quarter-Talbot plane $z = \frac{z_t}{4}$, the number of bright spots over the central loops is twice of the number of spots of the initial patterns at $z = 0$. Meanwhile, the contrast of the resulting quarter-Talbot images is minimum (see Visualization 1). These effects are fully consistent with self-imaging at the quarter-Talbot planes of the conventional Talbot effect [20,21]. Although the intensity patterns at $z = 0$ are nonseparable (in the polar coordinates), at the quarter-Talbot plane, the resulting pattern is separable after subtracting the background term. A similar effect was observed and investigated for the 2D orthogonal nonseparable periodic structures in Ref. [10]. The resulting 2D array of light spots over the self-image planes can be used for multi-trapping.

Now we consider a bit complicated structure that we will call binary-like single-frequency APBBS. Before defining the structure, we recall transmittance of a radial grating with a binary profile [12]:

$$t(\theta) = \frac{1}{2}\{1 + \text{sign}[\cos(m\theta)]\} = \frac{1}{2}\left[1 + \sum_{q=1}^{\infty} s_q \cos(qm\theta)\right],$$
(13)

where "sign" indicates the sign function that extracts the sign of a real number, m is the grating's spokes number, and

$s_q = \frac{4}{q\pi} \sin\left(\frac{q\pi}{2}\right)$. Using the Fourier expansion form of the transmittance in Eq. (13), we construct a binary-like single-frequency APBBS as follows:

$$t(r,\theta) = \frac{1}{2}\left[1 + a_m \sum_{q=1}^{\infty} s_q J_{qm}\left(\frac{2\pi r}{r_0}\right)\cos(qm\theta)\right],$$
(14)

where by setting $a_m = 1/\max\{\sum_{q=1}^{\infty} s_q J_{qm}(\frac{2\pi r}{r_0})\cos(qm\theta)\}$, the contrast of the transmittance can be maximized. Comparing Eqs. (14) and (7), we see that $c = \frac{1}{2}$, $t_{n=qm} = \frac{a_m s_q}{2}$, and other coefficients vanish $t_{n \neq qm} = 0$. Using these coefficients in Eq. (11), the near-field diffraction from sinusoidal APBBS can be obtained.

In Fig. 1(b), the transmittance of a binary-like single-frequency APBBS is illustrated. In Fig. 3, theoretically predicted and experimentally recorded diffraction patterns from two binary-like single-frequency APBBSs with $r_0 = 1$ mm and having two different $m = 3$ and $m = 10$ are illustrated.

Almost all the mentioned effects for Fig. 2 here again are apparent in Fig. 3 (see also Visualization 2).

At the last stage of the work, here, the theory of near-field diffraction from multi-frequency APBBSs is presented. We define a multi-frequency APBBS with the following transmission function:

$$t(r,\theta) = t_{00} + \sum_{l=1}^{\infty} \sum_{n=0}^{\infty} t_{ln} J_n\left(2\pi\sqrt{l}\frac{r}{r_0}\right)\cos(n\theta),$$
(15)

where r_0 is a characteristic length, and t_{ln} are arbitrary coefficients. In the passing of a coherent plane wave through this grating, the complex amplitude immediately after the grating is given by
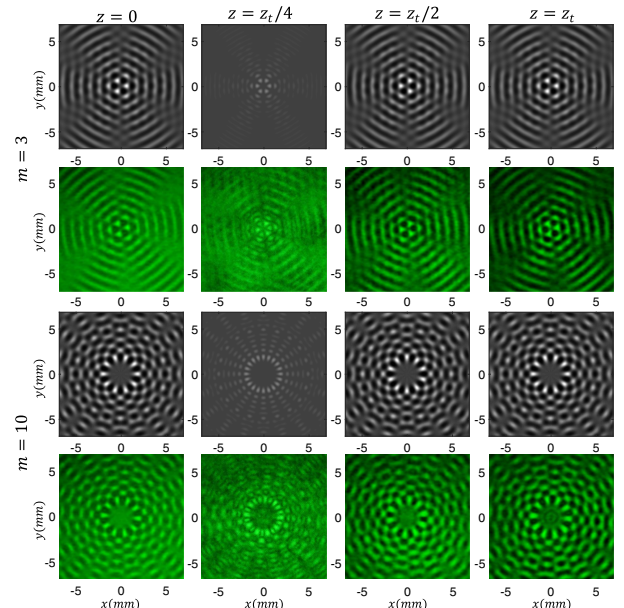

Fig. 3. Calculated (first and third rows) and experimentally recorded (second and fourth rows) intensity diffraction patterns at different propagation distances from binary-like single-frequency APBBSs with $r_0 = 1$ mm and having two different $m = 3$ and $m = 10$ (see Visualization 2).

$$\psi_0(r,\theta) = t_{00} + \sum_{l=1}^{\infty}\sum_{n=0}^{\infty} t_{ln}J_n(2\pi\rho_l r)\cos(n\theta), \qquad (16)$$

where $\rho_l = \sqrt{l}\rho_0$. The spatial spectrum of this amplitude distribution is obtained by taking a 2D Fourier transform of $\psi_0(r,\theta)$ as

$$\bar{\psi}_0(\rho,\varphi) = t_{00}\delta(\xi,\eta) + \sum_{l=1}^{\infty}\sum_{n=0}^{\infty} t_{ln}(-i)^n \cos(n\varphi)\frac{\delta(\rho-\rho_l)}{2\pi\rho_l}. \qquad (17)$$

This result shows that the spatial spectrum of the structure includes a point impulse on the origin of the spectrum domain and a set of concentric zone-plate-like circular-line impulses with radii of $\rho_l = \sqrt{l}\rho_0$ around the spectrum origin. Since the spectrum of the structure includes a set of radial spatial frequencies, we use the term "multi-frequency." The spatial spectrum of the light beam at a distance z from the structure is obtained by multiplying H to $\widetilde{\psi}_0(\rho,\varphi)$:

$$\bar{\psi}_z(\rho,\varphi) = t_{00}\delta(\xi,\eta)$$
$$+ \sum_{l=1}^{\infty}\sum_{n=0}^{\infty} t_{ln}e^{-i\pi\lambda z\rho_l^2}(-i)^n \cos(n\varphi)\frac{\delta(\rho-\rho_l)}{2\pi\rho_l}. \qquad (18)$$

Taking an inverse Fourier transform from $\widetilde{\psi}_z(\rho,\varphi)$, the near-field diffraction amplitude is calculated as

$$\psi_z(r,\theta) = t_{00} + \sum_{l=1}^{\infty}\sum_{n=0}^{\infty} e^{-2i\pi l\left(\frac{z}{z_t}\right)} t_{ln}J_n(2\pi\rho_l r)\cos(n\theta), \quad (19)$$

where $z_t = \frac{2}{\lambda\rho_0^2} = \frac{2r_0^2}{\lambda}$ can be considered as the structure's Talbot distance. Comparing Eqs. (16) and (19), we see that at distances equal to integer multiples of z_t, the diffracted amplitude fully recovers its initial shape. As an objective example, we define transmittance of a binary-like multi-frequency APBBS as follows:

$$t(r,\theta) = \frac{1}{2}\left[1 + a\sum_{l=1}^{\infty}\sum_{q=1}^{\infty}\frac{s_q}{l^2}J_{qm}(2\pi\rho_l r)\cos(qm\theta)\right], \quad (20)$$

where a is a constant maximizing the contrast. Here, two different types of binary-like multi-frequency APBBSs are considered; in the first type, l takes natural numbers, say $l = 1, 2, 3, \ldots$, and in the second type, l takes odd numbers, say $l = 1, 3, 5, \ldots$. The intensity patterns immediately after these structures and corresponding near-field diffraction patterns at different propagation distances are shown in Fig. 4. As is seen for the first type, the half-Talbot image has considerable difference, with the initial pattern especially at the center of pattern, but for the second type, these images are the same, only with a π phase shift (see also Visualization 3 and Visualization 4).

In summary, in this Letter, self-imaging in the polar coordinates for the APBBSs was investigated. Single- and multi-frequency APBBSs were defined, and the Talbot effect for these structures was formulated. The theory of near-field diffraction from sinusoidal and binary-like single-frequency APBBSs was presented and the results verified with the experiments. The produced arrays of intensity spots in the diffraction of plane waves from APBBSs may find applications in multi-trapping.
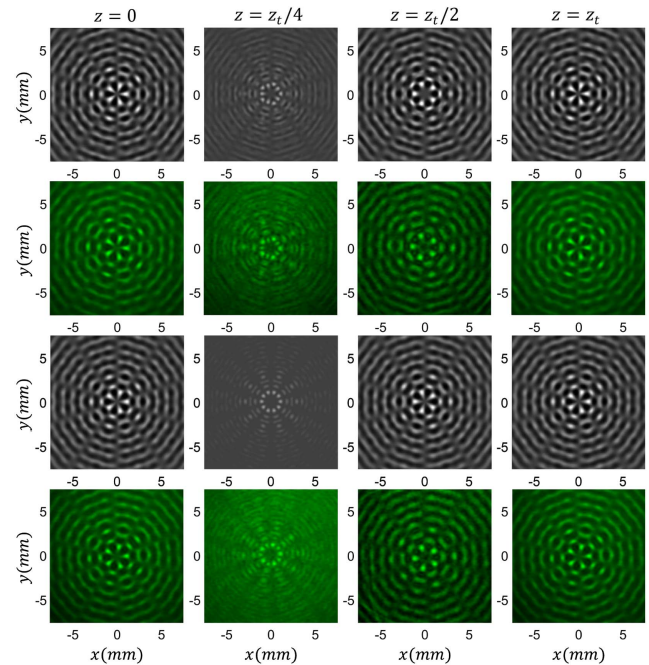

Fig. 4. Calculated (first and third rows) and experimentally recorded (second and fourth rows) near-field diffraction patterns at different propagation distances for the first type (first and second rows) and second type (third and forth rows) binary-like multi-frequency APBBSs with $r_0 = 1$ mm and $m = 5$ (see also Visualization 3 and Visualization 4).

REFERENCES

1. H. F. Talbot, Philos. Mag. **9**, 401 (1836).
2. W. D. Montgomery, J. Opt. Soc. Am. **57**, 772 (1967).
3. Rayleigh, Philos. Mag. **11**, 196 (1881).
4. K. Patorski, Prog. Opt. **27**, 1 (1989).
5. M. V. Berry and S. Klein, J. Mod. Opt. **43**, 2139 (1996).
6. J. Wen, Y. Zhang, and M. Xiao, Adv. Opt. Photon. **5**, 83 (2013).
7. A. W. Lohman and J. A. Thomas, Appl. Opt. **29**, 4337 (1990).
8. Z. Bouchal and J. Wagner, Opt. Commun. **176**, 299 (2000).
9. P. Szwaykowski, J. Opt. Soc. Am. A **5**, 185 (1988).
10. D. Hebri and S. Rasouli, J. Opt. Soc. Am. A **36**, 253 (2019).
11. H. Hsu, J. Weng, and P. Han, J. Opt. Soc. Am. A **36**, 270 (2019).
12. S. Rasouli, A. M. Khazaei, and D. Hebri, J. Opt. Soc. Am. A **35**, 55 (2018).
13. S. Rasouli, S. Hamzeloui, and D. Hebri, Opt. Express **27**, 17435 (2019).
14. D. Hebri, S. Rasouli, and M. Yeganeh, J. Opt. Soc. Am. B **35**, 724 (2018).
15. S. Rasouli, A. M. Khazaei, and D. Hebri, Phys. Rev. A **97**, 033844 (2018).
16. D. Hebri and S. Rasouli, Phys. Rev. A **98**, 003800 (2018).
17. Y. Y. Sun, J. Bu, L. S. Ong, and X.-C. Yuan, Appl. Phys. Lett. **91**, 051101 (2007).
18. J. W. Goodman, Introduction to Fourier Optics, 2nd ed. (McGraw-Hill, 1996).
19. J. D. Gaskill, Linear Systems, Fourier Transforms, and Optics (Wiley, 1978).
20. S. Rasouli and D. Hebri, J. Opt. Soc. Am. A **34**, 2145 (2017).
21. S. Rasouli, D. Hebri, and A. M. Khazaei, J. Opt. **19**, 095601 (2017).